Predicting Rubisco-Linker Condensation from Titration in the Dilute Phase

Alex Payne-Dwyer[1,*] Gaurav Kumar,[2,3,*] James Barrett[2,3,*] Laura K. Gherman,[2,4] Michael Hodgkinson,[2] Michael Plevin,[2,4] Luke Mackinder[2,3] Mark C. Leake[1,2] and Charley Schaefer[1,†]

[1]*School of Physics, Engineering and Technology, University of York, York, YO10 5DD, United Kingdom*
[2]*Department of Biology, University of York, York, YO10 5DD, United Kingdom*
[3]*Centre for Novel Agricultural Products (CNAP), Department of Biology, University of York, York, YO10 5DD, United Kingdom*
[4]*York Structural Biology Laboratory, The University of York; York, YO10 5DD, United Kingdom*

The condensation of Rubisco holoenzymes and linker proteins into "pyrenoids," a crucial supercharger of photosynthesis in algae, is qualitatively understood in terms of "sticker-and-spacer" theory. We derive semianalytical partition sums for small Rubisco-linker aggregates, which enable the calculation of both dilute-phase titration curves and dimerization diagrams. By fitting the titration curves to surface plasmon resonance and single-molecule fluorescence microscopy data, we extract the molecular properties needed to predict dimerization diagrams. We use these to estimate typical concentrations for condensation, and successfully compare these to microscopy observations.

Biopolymer networks are ubiquitous in nature as biomaterials such as silk [1,2] and artificial hydrogels [3], and fulfil vital physiological roles intra- and extracellularly [4,5], in particular as natural [6–10] and artificial [11] (multicomponent [10,12,13]) biomolecular condensates. Several emergent properties of self-assembly can be reproduced by models through interactions via linker molecules across a biopolymer network, often proteins with high levels of intrinsic disorder, which comprise "stickers" interspersed by "spacers" [7]. The most crucial molecular properties, the sticker binding affinity and the extensibility of the spacers, are both typically unknown. Consequently, the need for extensive simulation assays [14] imposes a practical challenge to falsifying or advancing the theory. In this Letter, we remedy this by deriving semianalytical solutions that enable the full parametrization in the dilute phase, as well as the computationally efficient calculation of dimerization diagrams.

As a model system we focus on the "pyrenoid," which is a phase-separated organelle found in the photosynthetic chloroplast of eukaryotic algae and some basal land plants [15–17]. Across species, the supercharging of photosynthesis relies on the crosslinking of the principal CO_2-fixing holoenzyme Rubisco (schematically represented by the cube in Fig. 1) by multivalent linkers, whose binding motifs may bind to eight specific sites on Rubisco [16,18]. Binding is reversible, as evidenced by the liquidlike properties of the pyrenoid that were found *in vivo* and *in vitro* by rapid internal mixing, fusion, and fission [19,20]. The most widely studied species is the model green alga *Chlamydomonas reinhardtii*, whose linker protein essential pyrenoid component 1 (EPYC1) has five "Rubisco binding motif" stickers [16,18] that facilitate multiplicit binding [21].

In the following, we will derive semianalytical partition sums for Rubisco monomers and dimers. We then use the monomeric partition sum to calculate titration curves that we fit to surface plasmon resonance (SPR) and single-molecule fluorescence microscopy (Slimfield) data. This yields quantitative values for the sticker binding energy ε and the Kuhn length of the spacers, l_K. We use these to calculate dimerization diagrams using the dimeric partition sum, and compare the theoretical predictions to microscopy observations of droplet formation.
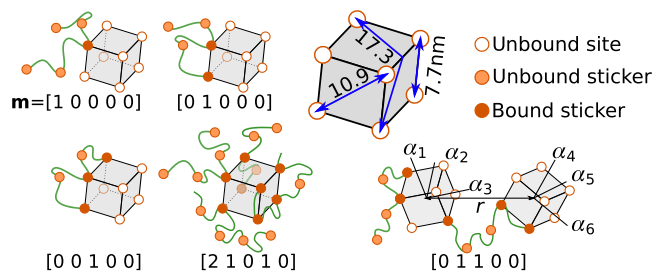

FIG. 1. Rubisco is parametrized using a cube with a space diagonal of 13.4 nm and whose corners represent binding sites (see SM). The permutations of linker binding are described using integer partitions' **m**, and the conformations using rotations $\boldsymbol{\alpha} = [\alpha_1, \ldots, \alpha_6]$ and center-to-center distance r.

Equilibrium self-assembly theory.—We model Rubisco as a cubic patchy particle [22] with at each corner a site to which stickers may bind with an energy ε. If stickers i and $j > i + 1$ bind to two sites at a distance z (see Fig. 1), where stickers $i < k < j$ are open, a strand of $n_{ij} = \sum_{k=i}^{j-1} n_k$ monomers is stretched, with n_k the number of amino acids between stickers $k - 1$ and k (we fix $n_k = 50$ in this Letter). The force-extension characteristics of intrinsically disordered proteins is known to be highly complex due to local electrostatics and excluded-volume interactions. Nevertheless, they are typically dominated by the finite extensibility and by the chain entropy, which we here capture for any $n \equiv n_{ij}$ strand using the freely jointed chain model [23–27] (Supplementary Materials (SM) Sec. S5A [33]),

$$\frac{G(z;n)}{k_{\mathrm{B}}T} = \frac{3}{2}\ln\left(\frac{2\pi\gamma bn}{3l_{\mathrm{K}}}\right) + \frac{bn}{l_{\mathrm{K}}}\left[\frac{1}{2}\left(\frac{z}{bn}\right)^2 - \ln\left(1 - \left(\frac{z}{bn}\right)^2\right)\right], \quad (1)$$

which describes the entropy of an extended random walk of nb/l_{K} Kuhn segments with a Kuhn length l_{K} that exceeds the step length $b = 0.36$ nm of individual amino acids. The Kuhn length is an apparent property in that it is affected by our tacit assumption of a so-called theta solvent in which random-walk statistics hold, while in a good solvent the potential would be softened by self-avoiding walk statistics, and which would be compensated by a smaller apparent Kuhn length [28]. Based on other works on polypeptides, we expect a value in the range of $l_{\mathrm{K}} = 0.36$ to 1.5 nm [1,29–31]. Finally, in Eq. (1) $k_{\mathrm{B}}T$ is the thermal energy, and γ a nonuniversal constant [27] that we set to unity to ensure a positive entropic penalty for any value for z.

To calculate titration curves and dimerization diagrams we will require the partition sum of single-Rubisco complexes, $Z^{(1)} = \sum_{M=0}^{N} e^{M\mu/k_{\mathrm{B}}T} Z_M^{(1)}$, and of dimeric ones $Z^{(2)} = \sum_{M=1}^{2N-1} e^{M\mu/k_{\mathrm{B}}T} Z_M^{(2)}$, with μ the chemical potential of the linkers. The index M represents the number of bound linker molecules, and may vary from 0 to the number of sites $N = 8$ for a Rubisco monomer, but from 1 to $2N - 1$ for a dimer as at least one linker must be bound to a at least two sites to dimerise two Rubiscos. The partition sum $Z_M^{(1)}$ can be written (derivation in SM Sec. S5C [33]) as

$$Z_M^{(1)} = Z_{\mathrm{trans}}^{(1)} Z_{\mathrm{rot}}^{(1)} \sum_{B=M}^{\min\{N,MS\}} e^{-B\varepsilon/k_{\mathrm{B}}T} Z_{M,B}^{(1)}, \quad (2)$$

with $Z_{\mathrm{trans}}^{(1)}$ and $Z_{\mathrm{rot}}^{(1)}$ the translation and rotational partition sums, and with

$$Z_{M,B}^{(1)} = \sum_{\mathbf{m} \in \mathcal{P}_{M,B}} \psi_{\mathbf{m}} \Omega_{\mathbf{m}}^0 \langle \exp(-G_{\mathrm{elas}}/k_{\mathrm{B}}T) \rangle_{\mathbf{m}}, \quad (3)$$

for B bound stickers. We have introduced $\mathcal{P}_{M,B}$ as the set of "integer partitions" [32], $\mathbf{m} \equiv [m_1, m_2, ..., m_S]$, whose elements m_b count the number of molecules that are bound using b stickers. The set is constructed (SM Sec. S6A [33]) by finding all values for which $\sum_b m_b = M$ and $\sum_b b m_b = B$ is obeyed. For each integer partition (for $S = 5$ there are 64 of them), the upper limit for the number binding configurations is

$$\Omega_{\mathbf{m}}^0 = \frac{N!}{(N-B)!} \prod_{b=1}^{S} \frac{1}{m_b!}\left(\frac{S!}{(S-b)!b!}\right)^{m_b}, \quad (4)$$

which is damped by the factor $\psi_{\mathbf{m}} \leq 1$ to correct for physically inaccessible states due to the overstretching of spacer strands. The final factor in Eq. (3), $\langle \exp(-G_{\mathrm{elas}}/k_{\mathrm{B}}T) \rangle_{\mathbf{m}}$, is the ensemble averaged Boltzmann factor due to the spacer entropy in Eq. (1). $\psi_{\mathbf{m}}$ and $\langle \exp(-G_{\mathrm{elas}}/k_{\mathrm{B}}T) \rangle_{\mathbf{m}}$ are obtained through numerical sampling (SM Sec. S6A [33]). Using these results, we will calculate titration curves as

$$\langle M \rangle = \frac{\sum_{M=1}^{N} M e^{M\mu/k_{\mathrm{B}}T} Z_M^{(1)}}{\sum_{M=0}^{N} e^{M\mu/k_{\mathrm{B}}T} Z_M^{(1)}}. \quad (5)$$

To calculate dimerization diagrams, we use the identify $f/(1-f) = Z^{(2)}/Z^{(2)\prime}$ with f the fraction of dimers and where $Z^{(2)}$ is calculated using

$$Z_M^{(2)} = \frac{\pi}{\lambda^3} e^{-M\varepsilon/k_{\mathrm{B}}T} \int \mathrm{d}r\, r^2 f_{\mathrm{ex}}(r) Q_M(\varepsilon) \frac{f_M(\varepsilon, r)}{1 - f_M(\varepsilon, r)}, \quad (6)$$

which is the partition sum for dimeric Rubisco with M bound linkers (SM Sec. S5D [33]). The prefactor π/λ^3 also appears in the monomeric state $Z_M^{(2)\prime}$ described below, and does not affect the fraction of dimers. For completeness, $\lambda = \sqrt{h^2/2\pi m k_{\mathrm{B}}T}$ is the thermal wavelength, with h Planck's constant and m the mass of Rubisco. In Eq. (6) we have integrated the rotational degrees of freedom of the dimer, while the axial vibrations are captured by the integral over the inter-Rubisco distance r. The internal vibrations due to the rotations of the individual Rubiscos are captured by the partition sums $Z_m^{(1)}$ that comprise $Q_M = (Z_{\mathrm{trans}}^{(1)})^{-2} \sum_{m=0}^{M} Z_m^{(1)} Z_{M-m}^{(1)}$. The latter, Q_M, describes the configurations of binding M molecules to two Rubisco holoenzymes *without* linking them into a dimer. The partition sum of this monomeric state represents only a fraction $1 - f_M(\varepsilon, r)$ of the total partition sum that includes both monomeric and dimeric states. Thus, $Q_M(\varepsilon) f_M(\varepsilon, r)/(1 - f_M(\varepsilon, r))$ represents the configurational partition sum of the dimeric states, which we obtain through simulations (SM Sec. S6C [33]) [37–41]. For short
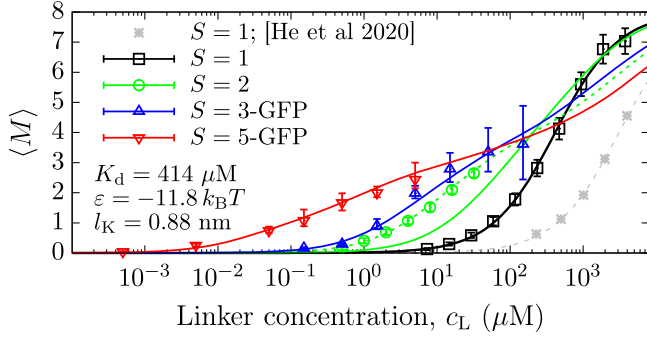
FIG. 2. The number of bound linkers, $\langle M \rangle$, against their concentration, c_{L}, for various numbers of stickers, S. The symbols are measured using SPR and Slimfield. The solid curves correspond to the best fit to the $S = 1, 3, 5$ data, and the dashed green curve is the best fit to the $S = 2$ data.

distances r, a fraction $(1 - f_{\mathrm{ex}})$ of the conformations is unavailable due to the intersection of the Rubiscos. We determine this factor numerically using the separating axis theorem in SM Sec. S6B [33]. If r approaches the contour length of the linker molecule, the integral converges to a constant value, i.e., the integral converges within a finite interval. To complete our calculation of the fraction of dimers f (rather than f_M), we calculate the monomeric partition sum as

$$Z_M^{(2)\prime} = \frac{\pi}{\lambda^3} e^{-M\varepsilon/k_{\mathrm{B}}T} \int \mathrm{d}r\, r^2 f_{\mathrm{ex}}(r) Q_M(\varepsilon)$$
$$= \frac{\pi}{\lambda^3} e^{-M\varepsilon/k_{\mathrm{B}}T} [V - V_{\mathrm{ex}}] Q_M(\varepsilon), \qquad (7)$$

where V is the system volume and $V_{\mathrm{ex}} \equiv \int \mathrm{d}r\, r^2 (1 - f_{\mathrm{ex}}(r))$ the excluded volume. Finally, to calculate dimerization diagrams, we substitute V for the Rubisco concentration $c_{\mathrm{R}}^0 = 2 \times 10^{30}/(V N_{\mathrm{A}})$ in units μM, with V in units nm³, and with $N_{\mathrm{A}} = 6.02 \times 10^{23}$ (mol⁻¹) Avogadro's constant.

Titration of linkers to single Rubisco.—To experimentally test the theory, we will parametrize the model using the concentration-dependent number of bound molecules $\langle M \rangle$ in Eq. (5) for various sequences, and compare predictions on condensation against microscopy observations. For these experiments, Rubisco was purified from *C. reinhardtii* [43], and EPYC1 variants with differing sticker numbers [$S = 1$, 2, 3, 4, 5, and green fluorescent protein (GFP) tagged 3-GFP, 5-GFP] were produced and purified from *E. coli* (SM Sec. S1 [33]) [44]. The $S = 1$ and $S = 2$ variants were used as analytes in SPR experiments in a buffer of 50 mM Tris-HCl and 50 mM NaCl at pH 8 (SM Sec. S2 [33]), in which Rubisco was immobilized on the chip surface and the binding response was determined across titration curves for each variant (Fig. 2). Variants of EPYC1 containing more than two stickers ($S > 2$) give rise to spontaneous phase separation of Rubisco at concentrations exceeding the critical concentration (SM Fig. S2 [33]) and therefore could
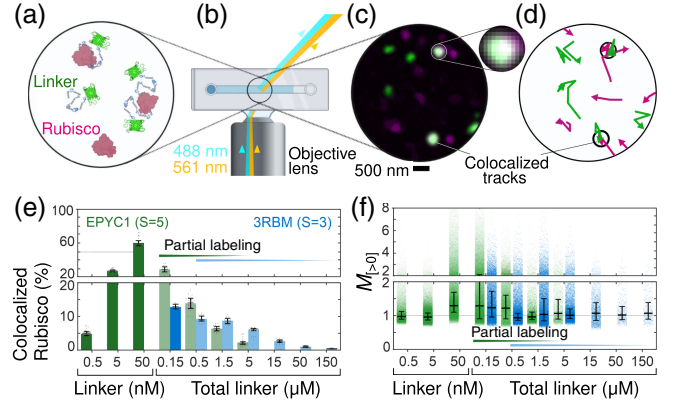

FIG. 3. Quantitative binding of linker and Rubisco using Slimfield. (a),(b) Rubisco-Atto594 is equilibrated with linker at mutual concentrations insufficient for phase separation, and introduced to a simple microscope chamber. (c) Slimfield reveals how assemblies of Rubisco (magenta, max projection) and/or linker GFP (green) adsorb transiently and nonspecifically to the cover glass. (d) Rapid molecular motion is reconstructed into tracks and unique colocalizations. (e) The fraction of individual Rubiscos with colocalized linker (means: EPYC1-GFP, green; 3RBM-GFP, blue; medians and interquartile range (IQR): black), θ, increases with visible linker. Partial labeling at total linker ≥ 150 nM masks the underlying binding curves. (f) Nonzero stoichiometries $M_{[>0]}$ of linker GFP at each Rubisco also rise with labeled linker (EPYC1-GFP, green; 3RBM-GFP, blue; medians/IQRs, boxes). The product of the two results is corrected for partial labeling to yield $\langle M \rangle$, which increases monotonically with total linker (Fig. 3).

not be used in SPR experiments due to their reliance on equilibrium binding.

Before we discuss the curve fits to the data, we now first focus on the titration curves for the $S = 3$ and $S = 5$ variants that we have measured using Slimfield microscopy (SM Sec. S4 [33]). Slimfield is a fluorescence microscopy technique that tracks protein assemblies at millisecond timescales in multiple colors and counts them with single-molecule sensitivity [45]. Coupled to bespoke tracking analysis [46], this technique examines and quantifies molecular dynamics *in vitro* [47] and *in vivo* [48]. We use this pipeline to identify and cotrack individual complexes of labeled Rubisco and/or linker near a coverslip surface without specific binding, at nanomolar concentrations [Figs. 3(a)–3(c)]. For these experiments we used the $S = 3$, 3-GFP,5, and 5-GFP EPYC1 variants, as well as Rubisco that was nonspecifically labeled with a fluorescent Atto594 dye. Here, our estimate of $\langle M \rangle$ follows from the expression $\langle M \rangle = \theta \langle M_{[>0]} \rangle / \phi_{\mathrm{GFP}}$, comprising two observable factors: θ, the fraction of detected single-Rubisco foci that are colocalized to linker foci, and $\langle M_{[>0]} \rangle$, the average apparent stoichiometry of those colocalized linker foci, then corrected for the visible molar fraction, ϕ_{GFP}, of linker GFP in total linker [49–52].

Low concentrations of Rubisco-Atto594 were used to ensure a dilute spatial distribution of isolated Rubisco foci

in the field of view [53], and mixed with excess linker at a range of total concentrations (0.5–50 nM linker at 5 nM Rubisco, and 150 nM–150 μM linker at 50 nM Rubisco). All experiments used the same buffers as in the SPR experiments. To maintain identifiable and distinct linker foci, the maximum linker-GFP concentration was fixed at 50 nM ($S = 5$-GFP) or 150 nM ($S = 3$-GFP), such that higher concentrations were diluted with the corresponding unlabelled linker ($10^{-3} < \phi_{GFP} < 1$). In each condition, $> 60\,000$ tracks each corresponding to a single molecule of Rubisco-Atto594 were detected from > 10 independent acquisitions [Fig. 3(d)].

For the native linker ($S = 5$) the proportion of colocalized Rubisco, θ, rises above 50% with linker concentration [Fig. 3(e)] indicating partial binding saturation. The concentration at which half of the Rubisco proteins are bound by at least one linker GFP lies between 5–50 nM [Fig. 3(e), green data], which resembles the binding affinity of 29 ± 12 nM estimated using fluorescence correlation spectroscopy [21]; see SM Fig. S9 [33]. At low labeling fractions ϕ_{GFP}, mostly isolated linker GFPs are observed at each Rubisco so that the binding response is largely encoded in θ/ϕ_{GFP}. The binding affinity is weakened for $S = 3$, and shifts this characteristic concentration to approximately 1 μM.

We have curve-fitted Eq. (5) to all titration curves obtained using SPR and Slimfield data in Fig. 2. For $S = 1$, Eq. (5) reduces to $\langle M \rangle = Nc_L/(K_d + c_L)$, with $K_d \propto \exp(\varepsilon/k_BT)$ the dissociation constant and $c_L = K_d \exp[(-\varepsilon + \mu)/k_BT]$ the concentration of unbound linkers (for low Rubisco concentrations this approximately equals the total concentration $c_L \approx c_{L,0}$). The curve fit to our SPR data of the 60-residue $S = 1$ fragment yielded $K_d = 414 \pm 52$ μM, and is smaller than the $K_d \approx 3$ mM of a 24-residue variant [16], albeit under different buffer conditions. By simultaneously fitting the model to our $S = 3$-GFP and $S = 5$-GFP data we found $l_K = 0.88 \pm 0.12$ nm and $\varepsilon = -11.8 \pm 0.8 k_BT$, which we have used to calculate all solid curves in Fig. 2. The variances are correlated through $\varepsilon \approx 11 l_K^{-0.45}$, and will be used in Fig. 4 to calculate confidence intervals on our predictions for dimerization concentrations. The $S = 2$ data displayed a higher binding affinity than expected, and was (nonuniquely) fitted using $\varepsilon \approx -12.7 l_K^{-0.55} k_BT$ (green dashed curve). It is inconclusive if this discrepancy is due to experimental factors (e.g., crosslinking of Rubisco at the surface; influence of fluorescent tags or coverslip, etc.), or if it may point at missing pieces of physics.

Condensation microscopy.—To calculate dimerization diagrams (SM Sec. S6D [33]) for linkers with $S = 2, 3, 4, 5$ stickers we have used $K_d = 414$ μM; $\varepsilon = -11.8 k_BT$, and $l_K = 0.88$ nm for the best fit to the single-molecule data in Fig. 2, and we have propagated the errors by using $(-12.5 k_BT, 0.75$ nm) and $(-11.0 k_BT, 1.0$ nm), as informed by the above-discussed relationship $\varepsilon = -11 l_K^{-0.45} k_BT$.
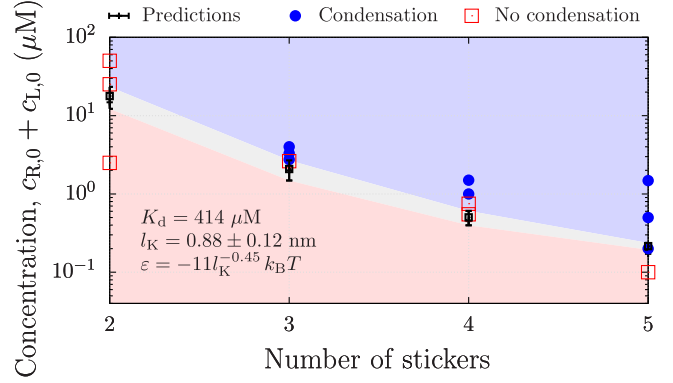

FIG. 4. Characteristic concentration for self-assembly against the number of stickers per linker molecule. The predictions are based on the best fit to the single-molecule data (black symbols) and the propagated uncertainty (gray shaded area). The microscopy observations are summarized by the open and closed symbols.

To calculate a characteristic concentration for condensation, we use the dimerization reaction as a proxy and approximate the "spinodal branch" by the condition where half of the material is dimerized, $f = 1/2$, and approximate the critical concentration by the "lower dimerization concentration" of Rubisco and linker for which this holds,

$$c = \min\{c_{R,0} + c_{L,0} | f(c_{R,0}, c_{L,0}) = 1/2\}. \qquad (8)$$

Figure 4 confirms that the characteristic concentration decreases with a decreasing Kuhn length in agreement with a simulation study on condensation [14].

To experimentally approximate the actual critical concentration for all untagged variants, we have performed condensation assays with a linker fraction fixed to $c_{L,0}/(c_{L,0} + c_{R,0}) = 0.88, 0.79, 0.68, 0.51$ for $S = 2, 3, 4, 5$, respectively, while the overall concentration $c_{L,0} + c_{R,0}$ was titrated until condensation was observed using microscopy (SM see S3 and Fig. S2). We compare the theoretical and the experimental values in Fig. 4.

We find striking agreement between the theory and experiments for the $S = 3$–5 constructs, indicating our simple framework does indeed have predictive value. However, for the $S = 2$ construct, which also showed distinct behavior in Fig. 2, we did not observe the formation of droplets. The predicted characteristic concentrations may be affected by some idealizations in our model, such as the cubelike particle affecting the intersite distances [14], or the (perhaps too) idealized force-extension model in Eq. (1). However, we speculate (anti-)cooperativity effects that emerge for clusters larger than dimers play a more crucial role. In particular, it is known that both biomacromolecules carry charges, which might be too weak to affect self-assembly in small systems, but which may add up in larger systems, and dictate finite sizes of the coacervate droplets [54]. We anticipate our dimerization diagrams may

inform concentration regimes of interest in large-scale simulations to address these open questions.

Conclusions.—We have crucially tested "sticker-and-spacer theory" by quantitatively comparing it to self-assembly properties both in the dilute and concentrated phase. The fits of the model to dilute-phase titration curves not only supports the theory, but also enables the measurement of both the sticker binding energy and the Kuhn length of the spacers. These allow for the prediction of dimerization diagrams, as well as a (crude) estimate for the critical point for condensation. By applying this approach to pyrenoids, we have found striking agreements for some linker variants, but also qualitative disagreements that point at open questions in the field. To arrive at these findings, we have developed semianalytical equations, numerical algorithms, and colocalization analyses in single-molecule microscopy; see SM [33]. We hope this pipeline to be of interest to the wider research on multicomponent sticker-spacer systems in soft matter science and the physics of life.

Data and code are available on [55].

---

[*]These authors contributed equally to this letter.

[†]Corresponding author: charley.schaefer@york.ac.uk

[1] C. Schaefer, P. R. Laity, C. Holland, and T. C. B. McLeish, Macromolecules **53**, 2669 (2020).

[2] C. Schaefer and T. C. B. McLeish, J. Rheol. **66**, 515 (2022).

[3] M. D. G. Hughes, B. S. Hanson, S. Cussons, N. Mahmoudi, D. J. Brockwell, and L. Dougan, ACS Nano **15**, 11296 (2021).

[4] C. Schaefer, G. H. McKinley, and T. C. B. McLeish, Interface Focus **12**, 20220058 (2022).

[5] Y. A. G. Fosado, J. Howard, S. Weir, A. Noy, M. C. Leake, and D. Michieletto, Phys. Rev. Lett. **130**, 058203 (2023).

[6] Y. Shin and C. P. Brangwynne, Cell. Biophys. **357**, 1253 (2017).

[7] J.-M. Choi, A. S. Holehouse, and R. V. Pappu, Annu. Rev. Biophys. **49**, 107 (2020).

[8] X. Jin, J.-E. Li, C. Schaefer, X. Luo, A. J. M. Wollman, T. Tian, X. Zhang, X. Chen, Y. Li, Y. Pu, T. C. B. McLeish, M. C. Leake, and F. Bai, Sci. Adv. **7**, eabh2929 (2021).

[9] J. Connor, S. Quinn, and C. Schaefer, Front. Mol. Neurosci. **15**, 962526 (2022).

[10] D. Qian, T. J. Welsh, N. A. Erkamp, S. Qamar, J. Nixon-Abell, G. Krainer, P. S. George-Hyslop, T. C. T. Michaels, and T. P. J. Knowles, Phys. Rev. X **12**, 041038 (2022).

[11] K. Lasker, S. Boeynaems, V. Lam, D. Scholl, E. Stainton, A. Briner, M. Jacquemyn, D. Daelemans, A. Deniz, E. Villa, A. S. Holehouse, A. D. Gitler, and L. Shapiro, Nat. Commun. **13**, 5643 (2022).

[12] T. S. Harmon, A. S. Holehouse, M. K. Rosen, and R. V. Pappu, eLife **6**, e30294 (2017).

[13] Y. Zhang, B. Xu, B. G. Weiner, Y. Meir, and N. S. Wingreen, eLife **10**, e62403 (2021).

[14] T. GrandPre, Y. Zhang, A. G. T. Pyo, B. Weiner, J.-L. Li, M. C. Jonikas, and N. S. Wingreen, PRX Life **1**, 023013 (2023).

[15] L. C. M. Mackinder, M. T. Meyer, T. Mettler-Altmann, V. K. Chen, M. C. Mitchell, O. Caspari, E. S. Freeman Rosenzweig, L. Pallesen, G. Reeves, A. Itakura, R. Roth, F. Sommer, S. Geimer, T. Mühlhaus, M. Schrodac, U. Goodenough, M. Stitt, H. Griffiths, and M. C. Jonikas, Proc. Natl. Acad. Sci. U.S.A. **113**, 5958 (2016).

[16] S. He, H.-T. Chou, D. Matthies, T. Wunder, M. T. Meyer, N. Atkinson, A. Martinez-Sanchez, P. D. Jeffrey, S. A. Port, W. Patena, G. He, V. K. Chen, F. M. Hughson, A. J. McCormick, O. Mueller-Cajar, B. D. Engel, Z. Yu, and M. C. Jonikas, Nat. Plants **6**, 1480 (2020).

[17] J. Barrett, P. Girr, and L. Mackinder, Biochim. Biophys. Acta Mol. Cell. Res. **1868**, 118949 (2021).

[18] M. T. Meyer, A. K. Itakura, W. Patena, L. Wang, S. He, T. Emrich-Mills, C. S. Lau, G. Yates, L. C. M. Mackinder, and M. C. Jonikas, Sci. Adv. **6**, eabd2408 (2020).

[19] E. F. Rosenzweig, B. Xu, L. K. Cuellar, A. Martinez-Sanchez, M. Schaffer, M. Strauss, H. Cartwright, P. Ronceray, J. Plitzko, F. Förster, N. Wingreen, B. Engel, L. Mackinder, and M. Jonikas, Cell **171**, 148 (2017).

[20] T. Wunder, S. Le Hung Cheng, S.-K. Lai, H.-Y. Li, and O. Mueller-Cajar, Nat. Commun. **9**, 5076 (2018).

[21] G. He, T. GrandPre, H. Wilson, Y. Zhang, M. C. Jonikas, N. S. Wingreen, and Q. Wang, Commun. Biol. **6**, 19 (2023).

[22] Z. Zhang and S. C. Glotzer, Nano Lett. **4**, 1407 (2004).

[23] M. Doi and S. F. Edwards, *The Theory of Polymer Dynamics* (Clarendon Press, Oxford, 1988).

[24] A. R. Khokhlov, A. Y. Grosberg, and V. S. Pande, *Statistical Physics of Macromolecules* (American Institute of Physics Melville, NY, 1994).

[25] A. Cohen, Rheol. Acta **30**, 270 (1991).

[26] J. M. Dealy, D. J. Read, and R. G. Larson, in *Structure and Rheology of Molten Polymers* (Second Edition), edited by J. M. Dealy, D. J. Read, and R. G. Larson (Hanser, 2018), pp. 461–533.

[27] J. D. Schieber, J. Neergaard, and S. Gupta, J. Rheol. **47**, 213 (2003).

[28] M. Rubinstein and R. H. Colby, *Polymer Physics*, 1st ed. (Oxford University Press, New York, 2003).

[29] S. Müller-Späth, A. Soranno, V. Hirschfeld, H. Hofmann, S. Rüegger, L. Reymond, D. Nettels, and B. Schuler, Proc. Natl. Acad. Sci. U.S.A. **107**, 14609 (2010).

[30] S. Cheng, M. Cetinkaya, and F. Gräter, Biophys. J. **99**, 3863 (2010).

[31] R. Zahn, D. Osmanović, S. Ehret, C. Araya Callis, S. Frey, M. Stewart, C. You, D. Görlich, B. W. Hoogenboom, and R. P. Richter, eLife **5**, e14119 (2016).

[32] I. Stojmenović and A. Zoghbi, Int. J. Comput. Math. **70**, 319 (1998).

[33] See Supplemental Material at http://link.aps.org/supplemental/10.1103/PhysRevLett.132.218401 for detail on the mathematical derivations (which includes Refs. [34–36]) and the experimental and numerical methods.

[34] M. E. Cates and V. N. Manoharan, Soft Matter **11**, 6538 (2015).

[35] E. D. Klein, R. W. Perry, and V. N. Manoharan, Phys. Rev. E **98**, 032608 (2018).

[36] R. Zangi, Phys. Chem. Chem. Phys. **24**, 28804 (2022).

[37] J. J. Lukkien, J. P. L. Segers, P. A. J. Hilbers, R. J. Gelten, and A. P. J. Jansen, Phys. Rev. E **58**, 2598 (1998).

[38] M. Saito and M. Matsumoto, in *Monte Carlo and Quasi-Monte Carlo Methods 2006*, edited by A. Keller, S. Heinrich, and H. Niederreiter (Springer Berlin Heidelberg, Berlin, Heidelberg, 2008), pp. 607–622.

[39] F. Haiping and A. Arcangeli (2012), https://github.com/forhappy/rbtree, commit:e1e984fcbc17d47a67652bb-c6276afe948c7ad55.

[40] D. W. Heermann and K. Binder, *Monte Carlo Simulation in Statistical Physics*, 5th ed. (Springer, Berlin, Heidelberg, 2010).

[41] A. P. J. Jansen, *An Introduction to Kinetic Monte Carlo Simulations of Surface Reactions*, 1st ed. (Springer-Verlag, Berlin Heidelberg, 2012).

[42] M. C. Lin, J. D. Cohen, and D. Manocha, *Proceedings of the 1995 Symposium on Interactive 3D Graphics* (1995).

[43] J. Kropat, A. Hong-Hermesdorf, D. Casero, P. Ent, M. Castruita, M. Pellegrini, S. S. Merchant, and D. Malasarn, Plant J. **66**, 770 (2011).

[44] R. B. Kapust, J. Tözsér, J. D. Fox, D. E. Anderson, S. Cherry, T. D. Copeland, and D. S. Waugh, Protein Eng. **14**, 993 (2001).

[45] M. Plank, G. Wadhams, and M. Leake, Integr. Biol. (Cambridge) **10**, 602 (2009).

[46] H. Miller, Z. Zhou, A. Wollman, and M. Leake, Methods **88**, 81 (2015).

[47] J. W. Shepherd, A. L. Payne-Dwyer, J.-E. Lee, A. Syeda, and M. C. Leake, J. Phys. Photonics **3**, 034010 (2021).

[48] A. Payne-Dwyer, A. Syeda, J. Shepherd, L. Frame, and M. Leake, J. R. Soc. Interface **19**, 20220437 (2022).

[49] M. C. Leake, D. Wilson, B. Bullard, and R. M. Simmons, FEBS Lett. **535**, 55 (2003).

[50] M. Leake, J. Chandler, G. Wadhams, F. Bai, R. Berry, and J. Armitage, Nature (London) **443**, 355 (2006).

[51] S. Torquato, B. Lu, and J. Rubinstein, J. Phys. A **23**, L103 (1990).

[52] M. C. Leake, Phys. Chem. Chem. Phys. **16**, 12635 (2014).

[53] T. C. Taylor, A. Backlund, K. Bjorhall, R. J. Spreitzer, and I. Andersson, J. Biol. Chem. **276**, 48159 (2001).

[54] S. Chen and Z.-G. Wang, Phys. Rev. Lett. **131**, 218201 (2023).

[55] C. Schaefer and A. Payne-Dwyer (2024), 10.5281/zenodo.10871144.